

A New Coordinated Control of Hybrid Microgrids with Renewable Energy Resources Under Variable Loads and Generation Conditions

Bilal Naji Alhasnawi*, Basil H. Jasim

Electrical Engineering Department, University of Basrah, Basrah, Iraq

Correspondence

*Bilal Naji Alhasnawi
Electrical Engineering Department,
University of Basrah, Basrah, Iraq
Email: bilalnaji11@yahoo.com

Abstract

The hybrid AC/DC microgrid is considered to be more and more popular in power systems as increasing loads. In this study, it is presented that the hybrid AC/DC microgrid is modeled with some renewable energy sources (e.g. solar energy, wind energy) in the residential of the consumer in order to meet the demand. The power generation and consumption are undergoing a major transformation. One of the tendencies is to integrate microgrids into the distribution network with high penetration of renewable energy resources. In this paper, a new distributed coordinated control is proposed for hybrid microgrid, which could apply to both grid-connected mode and islanded mode with hybrid energy resources and variable loads. The proposed system permits coordinated operation of distributed energy resources to concede necessary active power and additional service whenever required. Also, the maximum power point tracking technique is applied to both photovoltaic stations and wind turbines to extract the maximum power from the hybrid power system during the variation of the environmental conditions. Finally, a simulation model is built with a photovoltaic, wind turbine, hybrid microgrid as the paradigm, which can be applied to different scenarios, such as small-sized commercial and residential buildings. The simulation results have verified the effectiveness and feasibility of the introduced strategy for a hybrid microgrid operating in different modes

KEYWORDS: Distributed Coordination, Utility Grid, Inverters Converters, Hierarchical Control, Microgrids.

I. INTRODUCTION

The smart grid is the next generation of the traditional power system grids that depends on the two-way power flow and information transfer capabilities [1]. A conventional grid consists of power generation, control centers, distribution, transmission, and end-users [2]. A major benefit of the smart grid is that it increases the system's, sustainability, flexibility, reliability, and safety. In addition, it provides two-way communication services and enables the use of renewable energy resources. Telemetry and monitoring require the latest communication technology [3]. A small unit of the smart grid called the smart microgrid. The smart microgrid is a part of a power system that supplies the electricity to small areas and it has the ability to operate in either grid-connected or island mode. Smart microgrids provide consumers with improved monitoring and control and new service technologies [4].

Microgrids are part of the low voltage network, usually on the consumer side. The microgrid works in two modes, including modes connected to the network (on-grid) or the island (off-grid). In grid connection mode, the microgrid is

connected to the utility network via a common connection point (PCC). In islanded mode, the microgrid works separately whenever it is disconnected from the utility network [5]. The process of controlling the microgrid in island mode is a complex task because it requires multilevel control techniques to ensure that the frequency and voltage of microgrid are symbolic and to better improve the system's power quality.

The rest of this paper is organized as follows. Section II presents a description of the related works. Section III presents the mathematical model of the distributed hybrid generation system, Section IV presents the operation modes of the microgrid, Section V presents the control methods of the microgrids. Section VI presents the cases studies, Finally, Section VII concludes the paper.

II. RELATED WORKS

In this section, we review relevant research covering coordinate control strategies in the context of areas related to this work. In [6], a super-capacitor /hydrogen/wind/hybrid power system was proposed to coordinate different sources



This is an open access article under the terms of the Creative Commons Attribution License, which permits use, distribution and reproduction in any medium, provided the original work is properly cited.

© 2020 The Authors. Published by Iraqi Journal for Electrical and Electronic Engineering by College of Engineering, University of Basrah.

to make the power injected into the grid controllable. In this DC system, all power sources are connected to a common DC bus before being connected to the grid via the main inverter. However, the impact of variable load demand on the system, however, is not studied. Another microgrid structure consisting of a fuel cell and a photovoltaic array is proposed in [7]. The coordinated operation has been developed to control unit power and control unit feed flow to reduce the number of operating mode changes and increase system stability. A similar microgrid configuration was shown in [8]. In [9], centralized coordinated control was employed to equalize the state of charge even for different capacities of distributed energy storage systems. However, the disadvantage is that one point of failure in one of the communication links leads to the loss of the overall coordination of the system. The multi-master- slave-based control was proposed to provide rapid load sharing with consideration of distant groups, while the coupling of reactive and active powers problem appears in long transformation [10]. Another method, decentralized coordinated control for balancing the discharge rate of Energy Storage System, is an effective method to prevent overcurrent and unintentional outage of renewable energy sources units and to provide large stability margin and fast response in an islanded microgrid [11]. Wu and his colleagues proposed an autonomous active power control strategy to achieve decentralized power management without an external connection. In [12], independent control is implemented in each unit using multi-loop controllers to autonomously supply power only during peak load periods and keep power balance. However, these two control conditions are dependent on the photovoltaic system, while the various renewable energy sources are still not considered. Integrated cooperative control of photovoltaic and energy storage system is proposed based on voltage and frequency (or active power and reactive power) control, Maximum Power Point Tracking Control (MPPT), and energy storage system charge/discharge control [13].

The presented method has the following disadvantages:

- Several control strategies designs are based on the small-signal model. that's mean cannot guarantee global stability.
- Many existing models suffer from incomplete plant dynamics because they ignore the inner controller's impact on the control, thus affecting both the performance and stability of converters.
- The aforementioned methods have a synchronization process with a phase-locked loop (PLL) when renewable energy resources are integrated into the existing microgrids. Moreover, the stability analysis of the microgrids becomes more complex after the heterogeneous renewable energy resources are integrated.

To overcome the aforementioned difficulties, this paper proposes A new coordinated control of hybrid microgrids with renewable energy resources under variable load and generation conditions. we can summarize the main advantages of the proposed method as follows:

- 1) To the best of the authors' knowledge, this paper is the first to propose a hierarchical control for both frequency and voltage restoration of a grid-connected microgrid and islanded microgrid based on consideration of a complete nonlinear system model, irrespective of parametric disturbances and uncertainties.
- 2) In the case of frequency restoration, the distributed consensus-based control demonstrates the accuracy of power-sharing.
- 3) To overcome phase-locked loop (PLL) issues, a new coordinated control architecture is proposed in islanded AC microgrids including renewable energy resources units without PLL. We use conventional proportional-resonant (PR).
- 4) The maximum power point tracking (MPPT) technique is applied to both photovoltaics stations and wind farms to extract the maximum power from the hybrid power system during the variation of the environmental conditions.

III. DISTRIBUTED HYBRID ENERGY GENERATION SYSTEM

A. Modeling of PV Cell

Figure.1 illustrates the equivalent circuit based on the single diode model of PV cell which can be represented as a current source, diode, series resistance, and parallel resistance. The I-V characteristics of PV cell are described by the mathematical standard Equation which is [14]:

$$I = I_{ph;cell} - I_{0;cell} \left[\exp \left(\frac{q(V+IR_{s;cell})}{akT} \right) - 1 \right] - \frac{V+IR_{s;cell}}{R_{p;cell}} \quad (1)$$

Where:

I_{PH} , the cell is the photocurrent (A) of the PV cell which represents the current source,

I_d , the cell is the current (A) computed by the Shockley diode equation of PV cell,

I_0 , the cell is reversed leakage or the saturation current of the PV cell diode,

q is the electron charge ($1.602 \times 10^{-19} C$),

k is the Boltzmann's constant ($1.38 \times 10^{-23} J/K$),

T is the temperature of the diode measured in Kelvin (K),

R_s , the cell is the series resistance of PV cell (Ω),

R_p , the cell is parallel resistance of PV cell (Ω) and

If the series and parallel resistances of PV cells are not taken into account, then the model of the PV cell is the ideal model. Fig. 3 illustrates the I-V curve derived from Equation (1) for the ideal PV cell. It is noted that the net output cell current (I) results from the difference between I_{PH} , cell and $I_{d,cell}$ of PV cell [15,16].

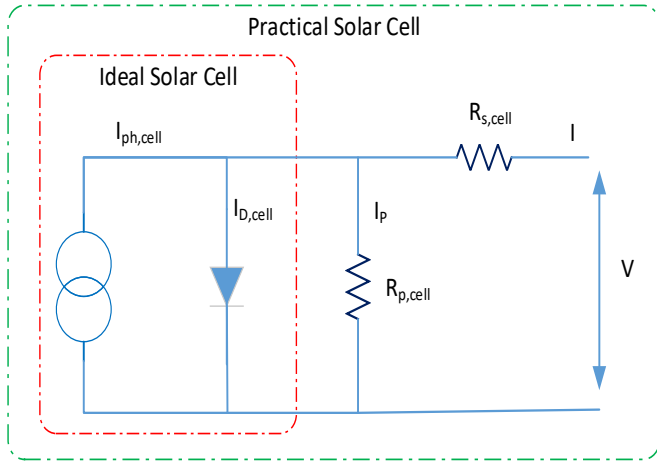


Fig. 1: The equivalent circuit of the PV cell

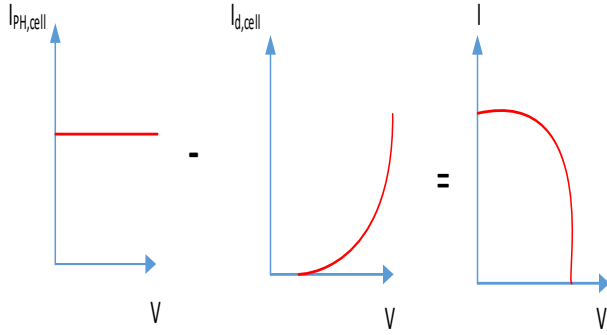


Fig. 2: A typical I-V curve of PV cell

B. Modeling of PV Module

As stated earlier, a PV module is composed of PV cells jointed in a series and parallel forms. Therefore, the mathematical standard Equation is derived from Equation (1) and the description of the I-V characteristic of the PV module becomes [17]:

$$I = I_{PH} - I_0 \left[\exp\left(\frac{V+IR_S}{aVt}\right) - 1 \right] - \frac{V+IR_S}{R_p} \quad (2)$$

where:

- I_{PH} is the photocurrent (A) of the module
- Vt is the thermal voltage of the module which is equal to $NskT/q$ where Ns refers to the number of series-connected cells,
- I_0 is reverse leakage current of the module,
- R_S is the series resistance of the module,
- R_p is the parallel resistance.

Equation (2) produces the I-V curve as indicated in Fig.3, where three salient points are bolded:

1. Short circuit current point ($0, I_{sc}$).
2. Maximum power point (MPP) (V_{mpp}, I_{mpp}) located at the V-I curve 's knee.
3. Open circuit voltage point ($V_{oc}, 0$).

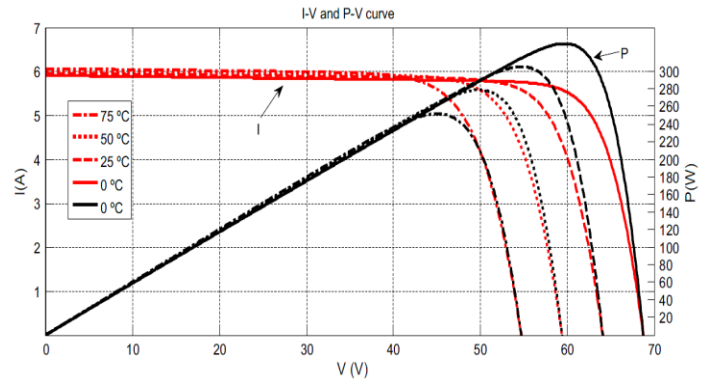


Fig. 3: I -V, P - V curves of a practical photovoltaic module at different temperature levels and constant insolation

The photocurrent of a PV module (I_{PH}) depends on the amount of the solar irradiance falling on the module and the PV cell temperature corresponding to the below Equation [18]:

$$I_{ph} = \frac{G}{G_n} (I_{ph,n} + Ki\Delta T) \quad (3)$$

where:

- $I_{PH,n}$ is the photocurrent under the nominal condition (usually $25C^0$ temperature and $1000W/m^2$ irradiance), ΔT is the difference between the actual temperature (T) and the nominal temperature (T_n) of the PV cell and they are measured in 0C ,
- G_n is the nominal irradiance ($1000 W/m^2$).
- G is the solar irradiance measured in W/m^2 ,
- Ki is the temperature coefficient.

While the open voltage circuit (V_{oc}) depends on the cell temperature corresponding to the below Equation:

$$V_{oc} = V_{oc,n} + K_v\Delta T \quad (4)$$

where:

- K_v is the temperature coefficient of the open-circuit voltage and $V_{oc,n}$ is the open-circuit voltage under the nominal conditions. The diode saturation current (I_0) can be obtained according to the below Equation:

$$I_0 = \frac{I_{sc,n} + K_t\Delta T}{\exp\left(\frac{V_{oc,n} + K_v\Delta T}{aVt}\right) - 1} \quad (5)$$

where $I_{sc,n}$ is the short circuit current under the nominal conditions [19].

C. Wind Turbine Model

Wind Turbines (WT) can be designed as an aerodynamic input torque that drives the DFIG. Fig. 4 shows the characteristic output curves of the wind turbine at different wind speeds. The mechanical strength (Pm) extracted from wind turbines can be expressed as [20].

$$P_m = \frac{1}{2} \rho A_t C_p(\lambda, \beta) V_w^3 \quad (6)$$

The performance factor of the wind turbine (C_p) depends on the blade aerodynamics and describes the efficiency of the

wind turbine. The performance factor (C_p) can be described as follows:

$$C_p(\lambda, \beta) = 0.5176 \left(\frac{116}{\lambda_i} - 0.4\beta - 5 \right) e^{-\left(\frac{21}{\lambda_i}\right)} + 0.0068\lambda \quad (7)$$

$$\frac{1}{\lambda_i} = \frac{1}{\lambda + 0.08\beta} - \frac{0.035}{\beta^3 + 1} \quad (8)$$

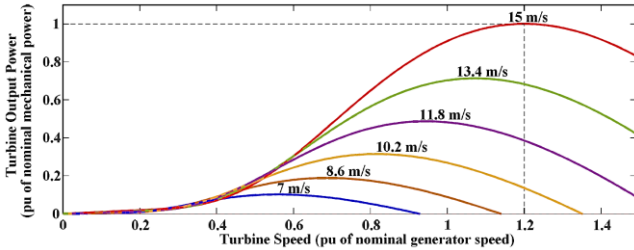


Fig. 4: Power characteristic curve for a wind turbine

IV. THE MICROGRIDS OPERATION MODES

This part describes the main operating modes. grid connection mode when there is an interaction with the utility network. islanded mode indicates a standalone operation, and the transient operation method, as the name implies, is a mode of transmission in the event of disconnection or restoration in connection with the main network [21].

A. Islanded Case

In this case, the connection to the utility grid is lost and the energy storage system plays an important role, which increases the operating costs of the system. Otherwise, the extra power cannot be saved. This case is more suitable for remote sites and is used mainly for seasonal purposes, as the local load is the only priority for this mode of operation. Since photovoltaic is the most cost-effective renewable energy resource technology, it represents most of the capacity of small island micro-grid. In the case of an island microgrids AC, the main focus of the transformer is not only multiple AC-DC-AC conversions but also it acts as a reference for voltage and frequency.

B. Grid-Connected Case

In this case, the microgrid is connected to the utility grid and all generating units operate at their maximum operational point. There are two modes of grid-connected connectivity. In the first situation, the priority of the grid-connected system is to meet local needs. In this mode, the surplus energy that can be generated in the micro-injection network can provide the shortfall through the main network. In the second grid-connection mode the only responsibility of the grid-connected microgrid is to aggregate generated power and supply it to the main network. The most important point in the operation of the microgrid in this situation is that the network operates a large network of a battery microgrid. Therefore, we can cover all the seasonal fluctuations of the load. There is a need to interface to connect the micro-network main network, but this situation adds to the total cost. The system can also operate in standalone mode in case of failure of process.

V. THE MICROGRID CONTROL METHODS

This part describes the microgrid control layer based on the hierarchical control method (primary, secondary, and tertiary). The base layer controls the device level and provides the fastest response, while the upper layers control the system level and slow down the response. To ensure energy quality and disruption in the microgrid network, the main features of the multi-layer control technology include filtering, harmonic current sharing, and reactive power, as well as control loops that regulate the flow of reactive and active power. By adjusting and providing stable voltage and frequency. To support the parallel operation of multiple voltage sources for network load sharing and power quality conservation, the overhang is mainly performed with hierarchical control [22, 23, 24].

A. The Primary Control Layer

A primary control layer, derived from the droop control method, is implemented to manage the power that each converter provides by regulating the frequency and voltage. The concept of drooping control originates from high power systems. This allows large, inertial large synchronous generators to operate in parallel with the combined load by reducing the frequency while increasing the active power in the grid. In contrast to typical traditional power systems, power generation units that are electronically coupled to the converters do not include inertial properties that provide stability to the system during the synchronization phase. Instead, it provides full control over system dynamics and transients by providing a very fast response. Therefore, to improve, microgrid stability, and coordination of voltage sources operating in parallel, the inertia properties of the synchronous generator are simulated electronically emulated in the network-forming converters by the droop method, regulating the frequency and voltage amplitude proportionally to the reactive and active power components [25]. The equations for the primary layer based on the droop control method are shown as in Equation (9) and Equation (10):

$$\omega_i = \omega_{nom} - m_i P_i \quad (9)$$

$$V_i = V_{nom} - n_i Q_i \quad (10)$$

Where ω_i is the angular frequency of the inverter i ($i = 1, 2, \dots, N$) corresponding to the measured active power P_i , ω_{nom} is the nominal frequency of the network, and m_i is the coefficient with respect to the active power for the droop method. On the other hand, V_i is the output voltage amplitude of the converter proportionally to the measured reactive power Q_i , V_{nom} the established nominal voltage amplitude, and n_i is the coefficient related to the reactive power for the droop method.

The frequency component is a global variable equally generated between the network-forming converters in steady-state, leading to an equally active power-sharing when the droop coefficient m_i is constant and equal for all inverters. Conversely, the voltage component is a local

variable, thus, even assuming similar droop coefficient n_i , there is no perfect reactive power sharing due to the uneven voltage amplitude in different nodes of the microgrid [26]. To show this, for two network-forming converters the reactive and active power sharing relations are shown in Equation (11) and Equation (12):

$$m_1 P_1 = m_2 P_2 \quad (11)$$

$$n_1 Q_1 = n_2 Q_2 + V_2 - V_1 \quad (12)$$

When the hierarchical control is not implemented, each converter injects dissimilar active power to the grid, depending on the line impedance detected at their nodes. The angular voltage and frequency from the droop equations are used to generate the sinusoidal voltage reference of each converter, as described in Equation (13):

$$V_{ref} = V_i \sin(\omega_i t) \quad (13)$$

To improve the dynamic transient response of the reference voltage, it is introduced a feed-forward component with respect to the active power in the angular frequency droop equation, as represented by Equation (14).

$$\omega_i = \omega_{nom} - m_i P_i - m_{ip} \frac{dP}{dt} \quad (14)$$

This droop compensation component is compatible with a proportional Derived Controller (PD). Here, the gain $m_i P_i$ contributes to a faster transient response regarding active power variations, and the derived term corresponds to the feed-forward signal. This parameter can improve the position of the system's closed-loop poles, increase damping characteristics and providing a higher variability

To reduce distortion, reduce the effects of circulating currents, and ensuring harmonic current sharing under non-linear and unbalanced loads, the drooping method emulates an impedance at the converter output through an additional closed-loop control. The default impedance is included in the voltage reference signal as a new variable based on the output current, as shown in Equation (15).

$$V_{ref} = V_i \sin(ph) - (R_v i_o + L_v \frac{di_o}{dt}) \quad (15)$$

where ph corresponds to the integral over time of Equation (14), i_o is output current of converter, L_v and R_v are the reactive inductive and resistive components of the virtual impedance Z_v , as shown in Equation (16):

$$Z_v = R_v + jL_v \quad (16)$$

The impedance variable is modified to provide mainly an inductive network, ensuring the controllability of the reactive and active power by the droop Equation (9) and Equation (10). Fig. 5 shows an output impedance loop regarding the droop control, voltage, and internal current loops.

The droop control applied in the primary control offers a satisfactory power balance among converters designed as network-forming. However, it introduces errors in the steady-state voltage and frequency. which is addressed by secondary control.

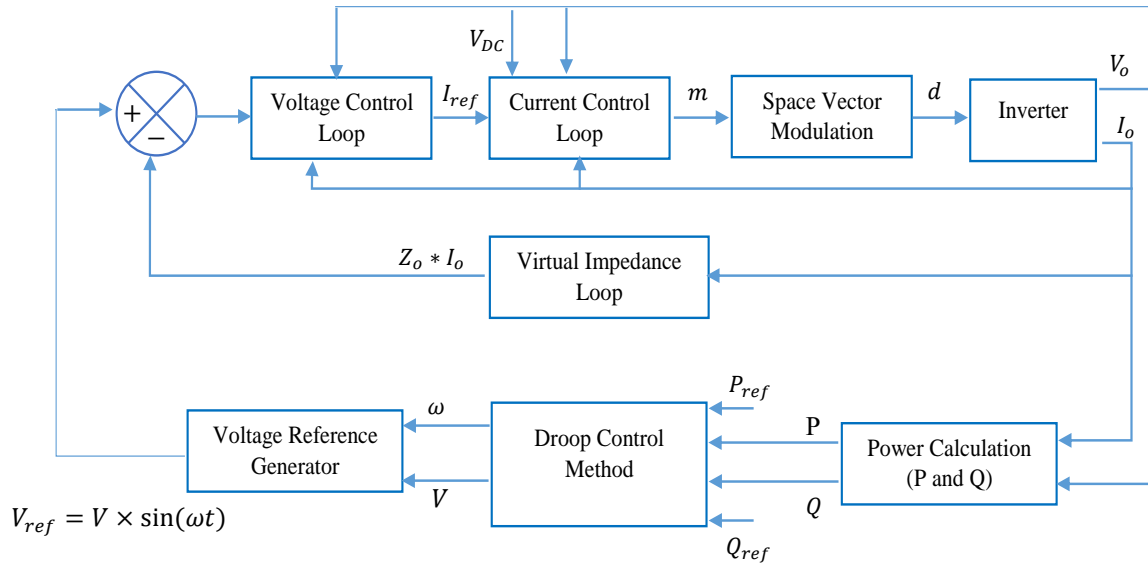


Fig. 5: Droop control with virtual output impedance control loop

B. The Secondary Control Layer

The secondary control layer reduces the deviations in voltage and frequency caused by the droop control in the steady-state, returns these values to a specific reference, and maintains the power-sharing achieved by the primary layer. In this layer, to restore frequency and voltage to their nominal values, add the term correction, and convert the drooping function to the initial properties of each unit. Fig.6 shows secondary and primary control procedures.

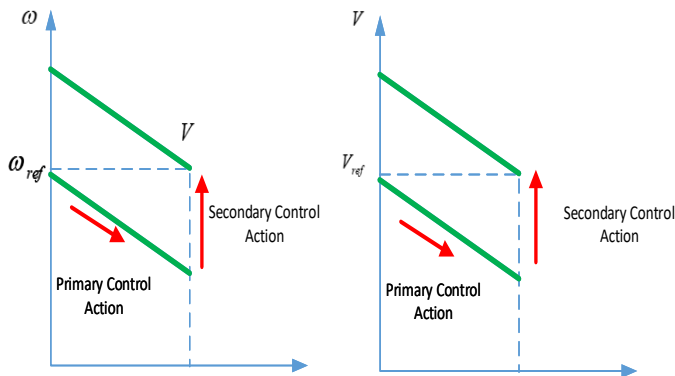


Fig. 6: Primary and secondary control actions

It should be noted that in the event that a secondary layer is not implemented, both the voltage and the frequency of the generation in the microgrid network depend on the load, with deviations due to the virtual inertia and impedances of the droop control in the primary layer. There are two secondary control techniques:

- 1) **Centralized Control:** Based on a central controller that requires one to all communication. The central controller uses measurements from the PCC (Point of Common Coupling) to calculate errors for all components and sends the corrective term to other converters. This is a robust approach to communication restrictions, but it is not reliable and has the flexibility and tolerance in case of converter failure.
- 2) **Decentralized Control:** A hybrid system based on local and central controllers, and requires one to all communication. As in the previous approach, the signal error is common in inverters obtained by the central controller, but properties as the corrective term are autonomously computed by each local controller. This technique is sensitive to communication issues since the inverters can produce different corrective terms if receiving information in distinct time due to non-synchronized internal clocks between controllers, an effect known as clock drift.

C. The Tertiary Control Layer

In this control layer, the power flow between the microgrid and the main grid is improved by independent power supply sensing and demand. Control of energy that is exported and imported from utility networks mainly depends on technical and economic issues such as tolerance of network errors, harmonic mitigation, interruption, and energy prices. Therefore, effective two-way communication to control power flow [27].

VI. CASE STUDY

The proposed hybrid AC/DC microgrid is realized in MATLAB. Simulation studies are carried out in accordance with various conditions as follows:

- **First case study:** The grid-connected (on-grid) mode microgrid composed by one renewable energy resources and one network converter and home load
- **Second case study:** The islanded (off-grid) Mode microgrid composed by one renewable energy resource and one network converter and home load (including the primary control only).
- **Third case study:** The islanded (off-grid) Mode microgrid composed by two renewable energy resources and two network converters and common home load (the primary control and the secondary control).

A- The first case: The grid-connected (on-grid) Mode microgrid composed by one renewable energy resources and one network converter and home load:

The first case study presents the grid-connected operation method with one renewable energy sources (photovoltaic system with maximum power point tracking control) and one inverter connected in parallel with one home (load). In this operating mode, the utility grid determines the phase, frequency, and amplitude of the voltage. Therefore, the main purpose of this case is to control the reactive and active power imported into the main network and exported it to the main network by adjusting the modulating signal produced in the inner current loop.

Table 1 shows the modified electrical parameters for the microgrid network under the first case study. Nominal voltage and DC link voltage definitions based on the physical properties of the buck converter with step-down behavior. Table.2 shows the standard voltage range.

TABLE 1
The Parameters of Microgrid Under First Case Study

Parameter	Acronym	Value	Units
AC Voltage	V_{nom}	220	V
Frequency	f_{nom}	50	Hz
Angular frequency	ω_{nom}	$2\pi \times f_{nom}$	Rad/s
DC-link voltage	V_{DC}	800	V
Load resistance	R_L	22	Ω
Load inductance	L_L	5	m H
Grid resistance	R_g	65	m Ω
Grid inductance	L_g	1	m H
Output inductance	L_{o1}	5	m H
Output resistance	R_{o1}	0.5	Ω
LC filter capacitance	C_{f1}	10	F
LC filter damping resistor	R_{f1}	20	Ω
Line inductance	L_{L1}	1	m H
Line resistance	R_{L1}	65	m Ω

TABLE 2
The DC-Link Range Voltage and AC Range Voltage

DC-Link voltage(V)	AC voltage (V)
350-650	110
650-850	220

The equations used to define these parameters are described as Equation (17).

$$P = \frac{3 \times V_{AC}^2}{R_L} \quad (17)$$

From Equation (17), the active power output is about 7 kW, and according to Equation (18), the current is about 10 A

$$I = \frac{P}{3V_{AC}} \quad (18)$$

Considering the approximation mentioned in Equation (19), for L_{o1} is equal to 5 mH, the per-unit value calculated is between the acceptable range, corresponding to 0.07:

$$Z = \frac{V_{AC}}{I} \approx R_L \gg \gg \gg \frac{(\omega_{nom} \times L_{o1})}{Z} = 0.7 \quad (19)$$

Impedance values at the output of the converter, local, and gridlines characterize the effects of power cable losses, network configuration, and parasitic elements of the power cables. The defined values detailed in Table 2.

The converter output interfaces with the load via a filter. The values of the damping resistor and shunt capacitor are adjusted to reduce noise and improve power output during disturbances in the load current. The low impedance of the filter capacitors provides a bypass the harmonic by switching the harmonic currents from the converter, preventing them to enter into the load. Table 3 lists the control parameters that apply to the first case study. The cut-off frequency value is added on a low pass filter (LPF), which is implemented to reduce harmonics and noise at output voltage and power signals.

TABLE 3
The Parameters of Microgrid Control

Parameter	Acronym	Value	Unit
Sampling rate	t_s	1	Second
Cut-off frequency LPF	ω_c	$0.03 \times \omega_{nom}$	Rad/second
Proportional gain PI dynamic active power reference	K_{pp}	0	A^{-1}
Integral gain PI dynamic active power reference	K_{ip}	0.5	$(As)^{-1}$
Proportional gain PI dynamic reactive power reference	K_{pq}	0	A^{-1}
Integral gain PI dynamic reactive power reference	K_{iq}	0.5	$(As)^{-1}$
Proportional gain current compensator	K_{pi}	12	A^{-1}
Integral gain current compensator	K_{ii}	200	$(As)^{-1}$
Damping coefficient current compensator	sh_i	0.1	

The cutoff frequency specified follows the rules defined in [6]. This indicates that this frequency should be between one to two decades lower than the nominal frequency, to ensure the slow transient response, and noise rejection, one desirable characteristic in electrical power systems. The design of the control parameters for the compensators mainly

depends on different operating points, sampling rates, and power ranges.

In all case studies, the specific control values were equivalent and adjusted during the simulation run based on the core function and characteristics of each parameter. Fig. 7. shows the scheme of the microgrid of the first case study.

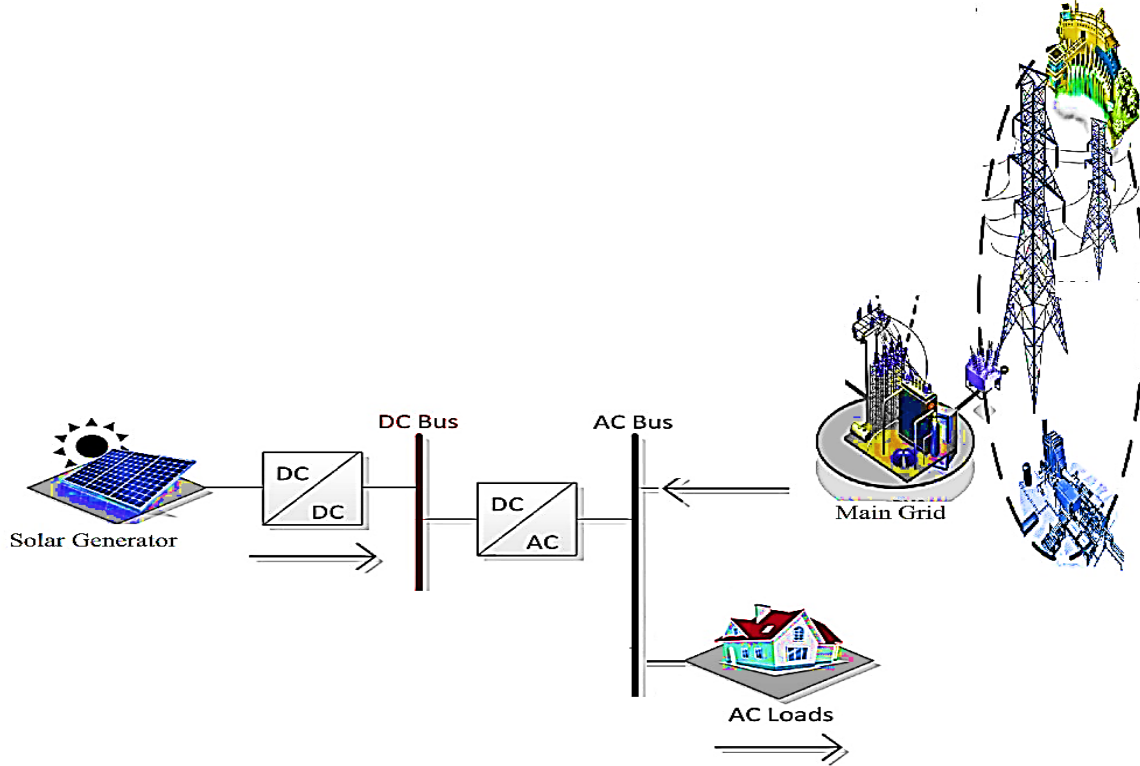


Fig. 7: The proposed system structure for the first case

The three-dimensional phasor terms are represented by means of $\alpha\beta$ -frame components, shown as in Equation (20) by the simplified transform of balanced systems, defined by the Clarke Transform [28]:

$$\begin{bmatrix} f_{\alpha}(t) \\ f_{\beta}(t) \end{bmatrix} = \frac{2}{3} \begin{bmatrix} 1 & -1/2 & -1/2 \\ 0 & \sqrt{3}/2 & -\sqrt{3}/2 \end{bmatrix} \begin{bmatrix} f_a(t) \\ f_b(t) \\ f_c(t) \end{bmatrix} \quad (20)$$

The sinusoidal functions and amplitude of the $\alpha\beta$ reference frame are expressed as in Equation (21), Equation (22), and Equation (23):

$$\hat{f}(t) = \sqrt{f_{\alpha}^2 + f_{\beta}^2} \quad (21)$$

$$f_{\alpha}(t) = \hat{f}(t) \cos[\theta(t)] \quad (22)$$

$$f_{\beta}(t) = \hat{f}(t) \sin[\theta(t)] \quad (23)$$

The $\alpha\beta$ frameworks are also implemented to convert current components defined as I-alpha and I-beta, which Combination with V-alpha and V-beta is the variable

responsible for controlling the active and reactive power signals represented by Equation (24) and Equation (25).

$$p = \frac{3}{2} (v_{\alpha} i_{\alpha} + v_{\beta} i_{\beta}) \quad (24)$$

$$q = \frac{3}{2} (-v_{\alpha} i_{\beta} + v_{\beta} i_{\alpha}) \quad (25)$$

Includes output voltage and power components LPFs (Low Pass Filter) for harmonic and noise mitigation. The Laplace for each element is represented by Equation (26), Equation (27), and Equation (28).

$$V_o(s) = v_o(s) \times \frac{w_c}{s+w_c} \quad (26)$$

$$P(s) = p(s) \times \frac{w_c}{s+w_c} \quad (27)$$

$$Q(s) = q(s) \times \frac{w_c}{s+w_c} \quad (28)$$

1. The Results of the First Case

The results of simulation for current tracking, modulated signal, instantaneous grid voltage, output voltage response, and power components are shown in Fig. 8, Fig. 9, Fig. 10, Fig. 11, Fig. 12.

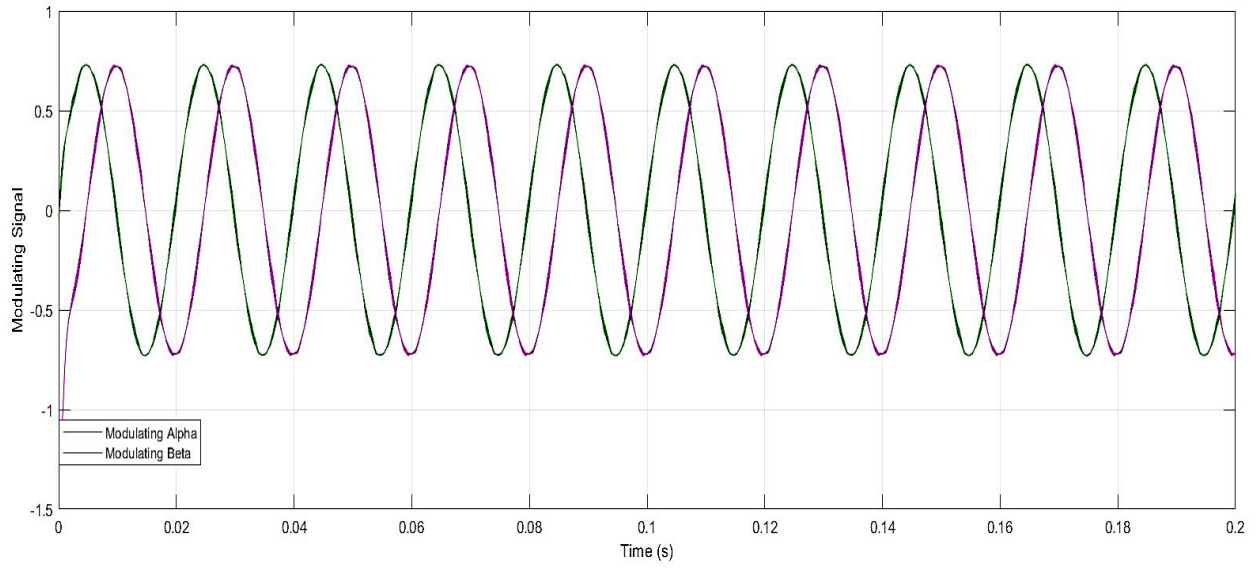


Fig. 8: The results of the modulating signals alpha and beta

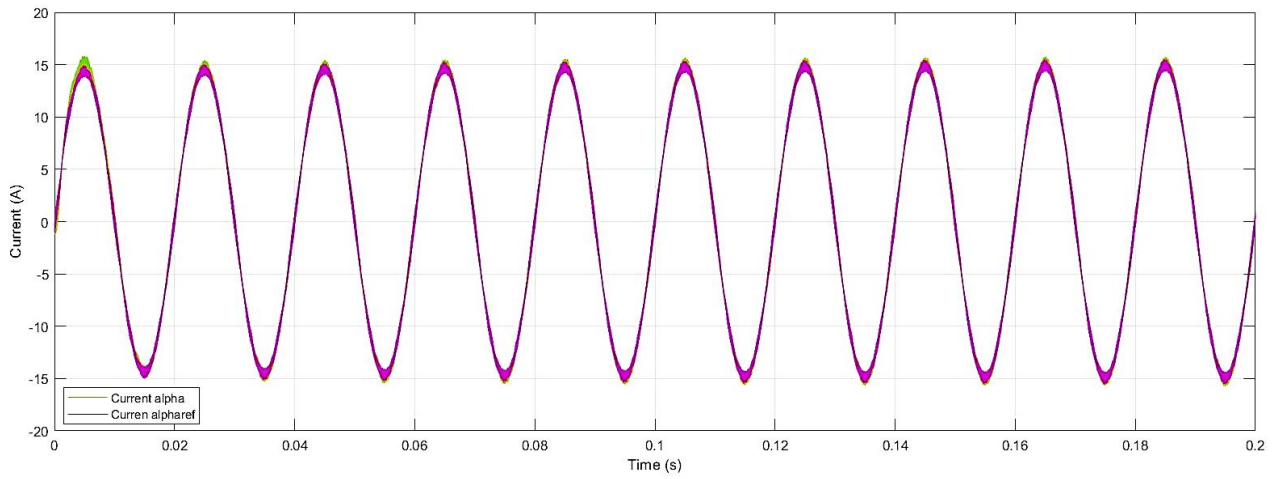


Fig. 9: The results of the current tracking from the current control

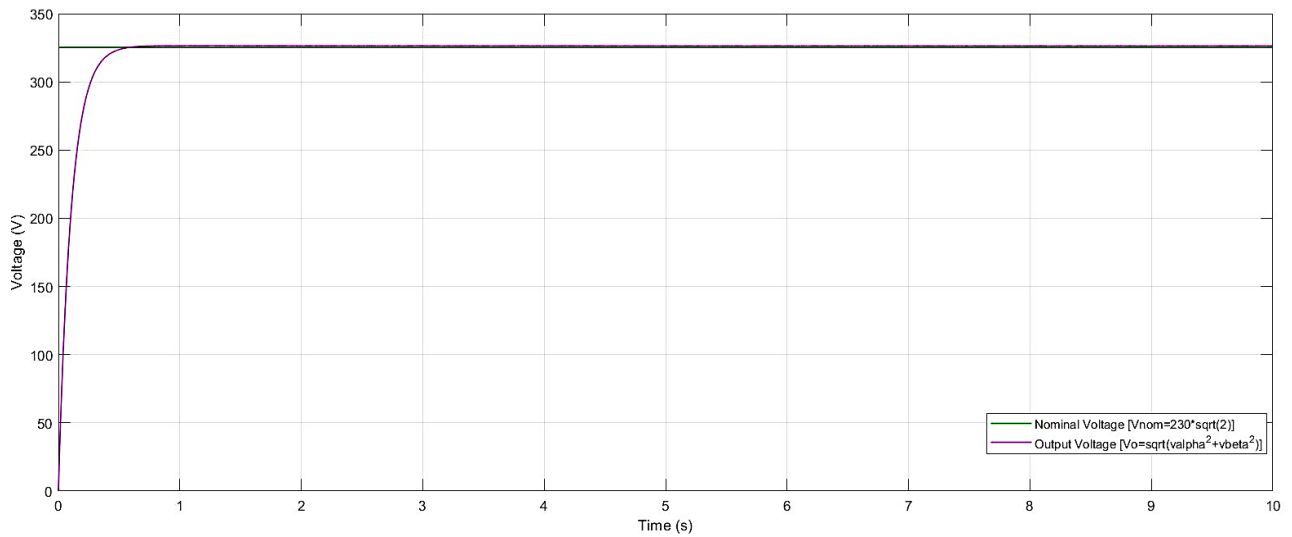


Fig. 10: The compare between the nominal and output voltage

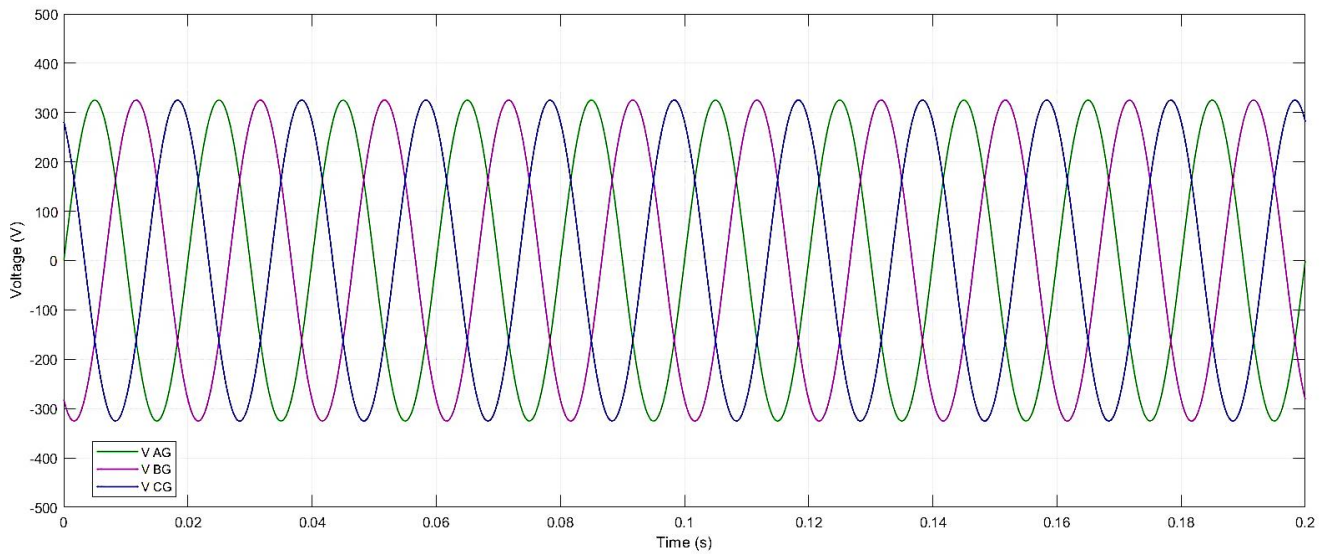


Fig. 11: The results of the grid voltage

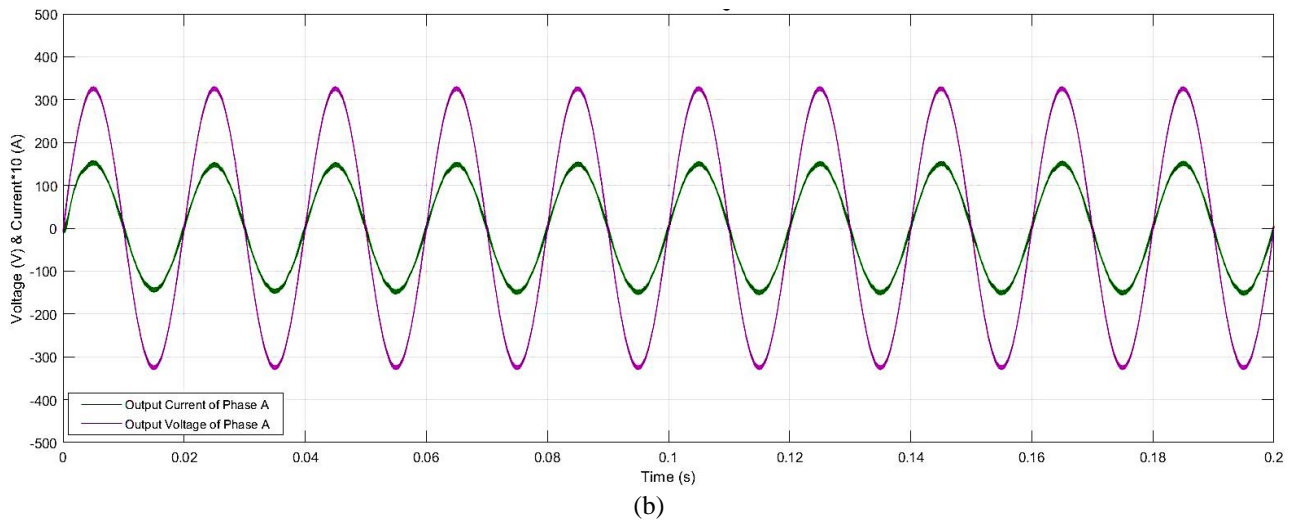
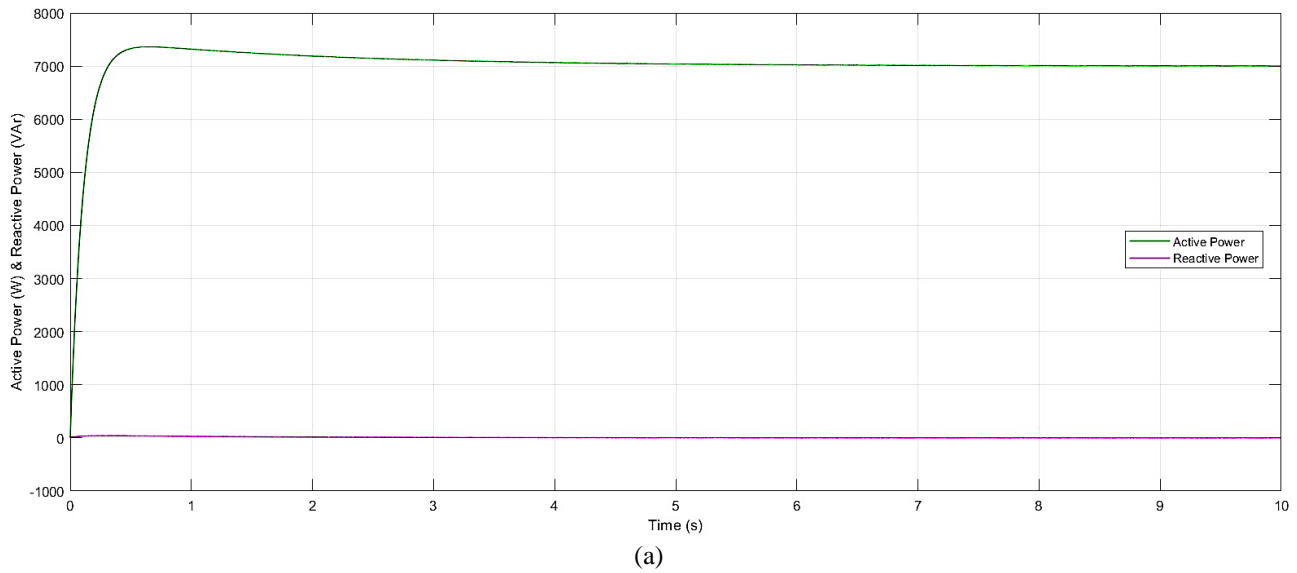


Fig. 12: The results of 7 kW and 0 kVAr, (a) Active and reactive power curves, (b) The voltage and the current

The modulating signal from Fig. 8. provides an accurate response via presenting the alpha leading the beta component by 90° ($\pi/2$). Fig. 9. proves the effective operation of the current control, in which the alpha current component follows the reference current established by the power control based on the output voltage measured values and the specified reactive and active power. The results shown in Fig. 10 illustrate the stable operation of the system. This achieves satisfactory signal performance for voltage response and reaches its nominal value. The grid voltage shown in Fig. 11 shows a perfectly balanced sinusoidal system with a constant frequency.

B- The Second Case Study: The islanded (off-grid) Mode microgrid composed by one renewable energy resource and one network converter and home load (including the primary control only).

In islanded mode, the microgrid is not connected to the power utility grid due to a pre-planned or nonplanned event,

in which case the network feeder is provided by network-forming converters. The second case study shows the off-grid mode with one inverter operating and one local load.

Therefore, the purpose of this study is to implement the internal current loop control and the outer voltage loop control based on the droop control that adjusts the frequency and voltage with respect to reactive and active power. Table.4 shows the parameters specified for the second case study. The droop control slopes m_p and n_q are defined to optimize voltage and frequency with reference to reactive and active power. The design of the compensator's gains can be based on the relation expressed by Equation (29) and Equation (30):

$$m_p = \frac{\Delta f}{P_{max}} \quad (29)$$

$$n_q = \frac{\Delta f}{2Q_{max}} \quad (30)$$

TABLE 4
The Control Parameters of Microgrid in Second Case

Parameter	Acronym	Value	Unit
Frequency droop parameter	m_p	130	Rad/Ws
Frequency droop derivative parameter	m_{pp}	10	Rad/W
Voltage droop parameter	n_q	1	m V/VAr
Droop method impedance	L_v	1	Mh
Droop resistance	R_v	0	Mh
Proportional gain voltage compensator	K_{pv}	0.1	A/V
Integral gain voltage compensator	K_{iv}	0.1	A/(Vs)
Damping coefficient voltage compensator	sh_{iv}	0.01	

As explained in Equation (31) and Equation (32), it depends on the statement that a dominant inductive characteristic can be satisfactorily ensured by any impedance angle higher than 65°

$$\theta = \tan^{-1} \left(\frac{\omega_{nom}(L_v+L_g)}{R_v+R_g} \right) > 65^\circ \quad (31)$$

$$\left(\frac{\omega_{nom}(L_v+L_g)}{R_v+R_g} \right) > 2.14 \quad (32)$$

Where R_g and L_g are resistive and inductive grid components, R_v and L_v are resistive and inductor impedance components.

The compensator parameters are tuned based on their characteristics. the proportional gain provided a fast transient response and it was set to a small value since it can distort the signal rapidly, while integrated gain presents a slow and smooth response. Figure.13 illustrates the microgrid of case 3. The microgrid scheme of case 3 consists of one network-forming converter modeled in series with one AC Home (load).

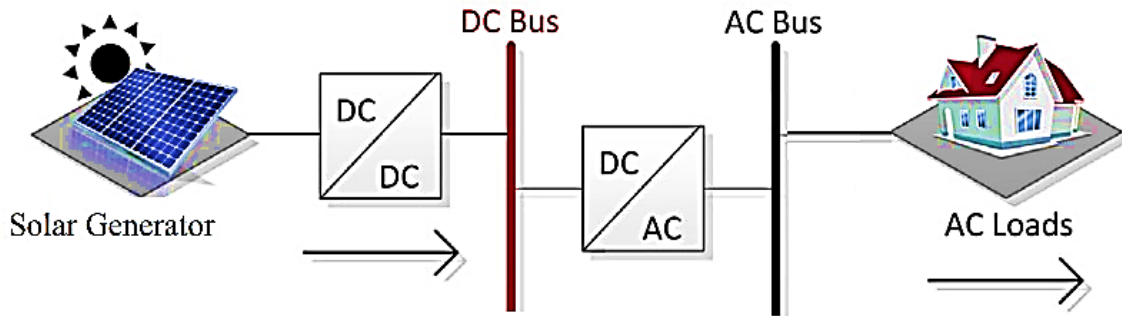


Fig. 13: The proposed system structure for the second case

The designed parameters are derived from the expressions defined in Equation (15) and Equation (16). Due to the 90° lagging of the β to the α signal, the time derivative term is determined by cross-coupling, as defined in Equation (33) and Equation (34) [6]:

$$Z_v I_{o\alpha} = R_v I_{o\alpha} + \omega_{nom} L_v I_{o\beta} \quad (33)$$

$$Z_v I_{o\beta} = R_v I_{o\beta} - \omega_{nom} L_v I_{o\alpha} \quad (34)$$

1. The Results of the Second Case

The results for the modulating signal, current, and voltage tracking, reactive and active power are illustrated in Fig. 14, Fig. 15, Fig. 16, Fig. 17, Fig. 18, and Fig. 19.

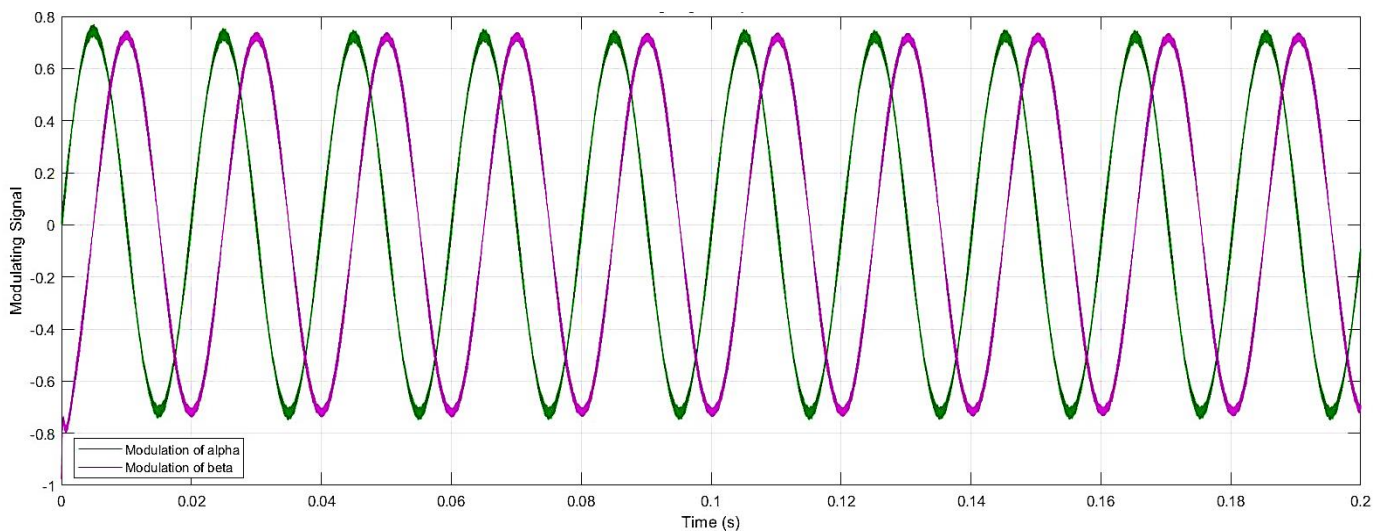


Fig. 14: The results of modulating signals alpha and beta

Figure 14 shows that the alpha leading the beta component by 90° ($\pi/2$), which confirms the precise response of the modulated signal. Figure 15 validates the current trace of the generated alpha component over the reference value defined by the current control. The voltage tracking from the voltage control shown in Fig. 16 illustrates precise operation based on the measured output voltage and line current components. Since the load is mainly resistive, the reactive power

component present in Fig. 17 is approximately equal to zero, but the active power corresponds to the estimate in Equation (2.1). The results obtained in Fig. 18 indicate stable system operation, which reaches the voltage nominal value. Figure 19 shows that by applying only the primary control, the output frequency response presents a steady-state error that requires a secondary control to restoration purposes.

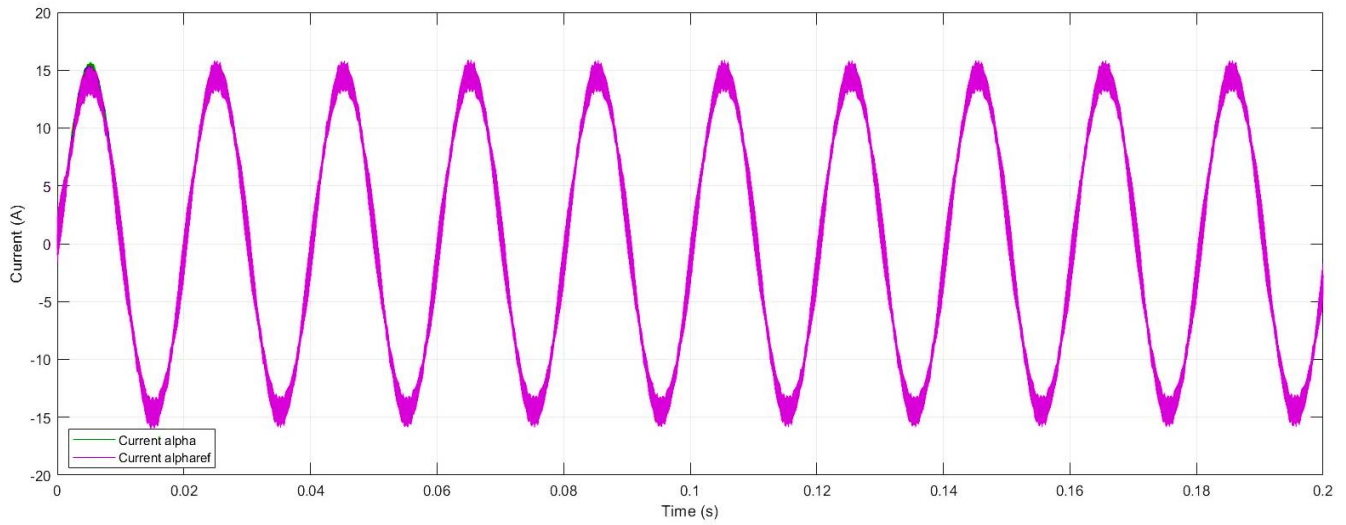


Fig. 15: Results of the current tracking from the current control (Case Study 2)

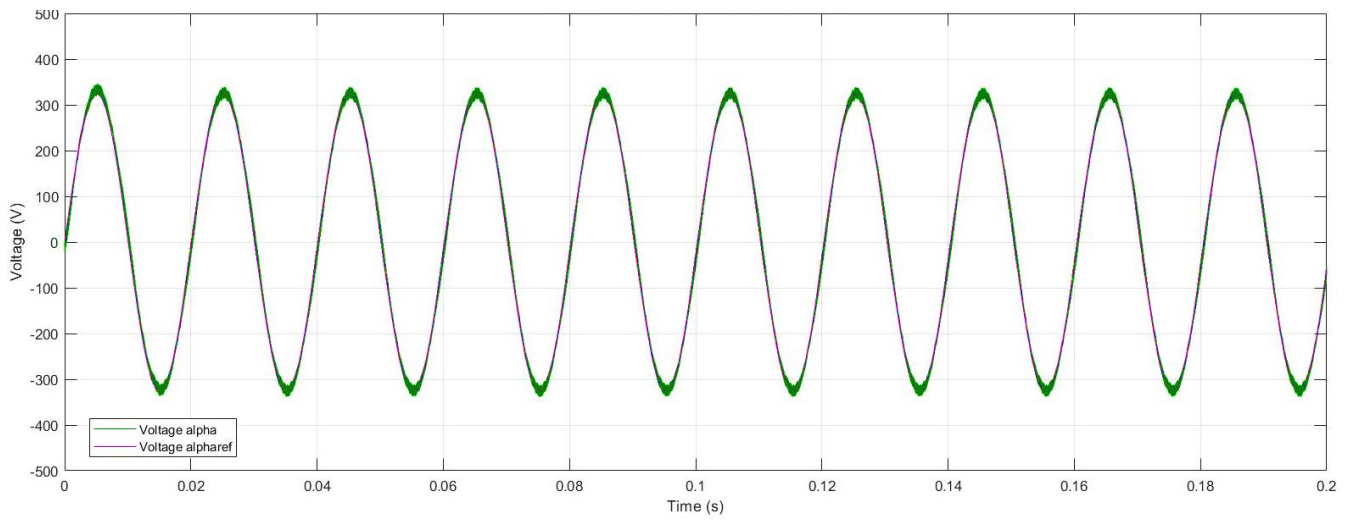


Fig. 16: Results of the voltage tracking from voltage control (Case Study 2)

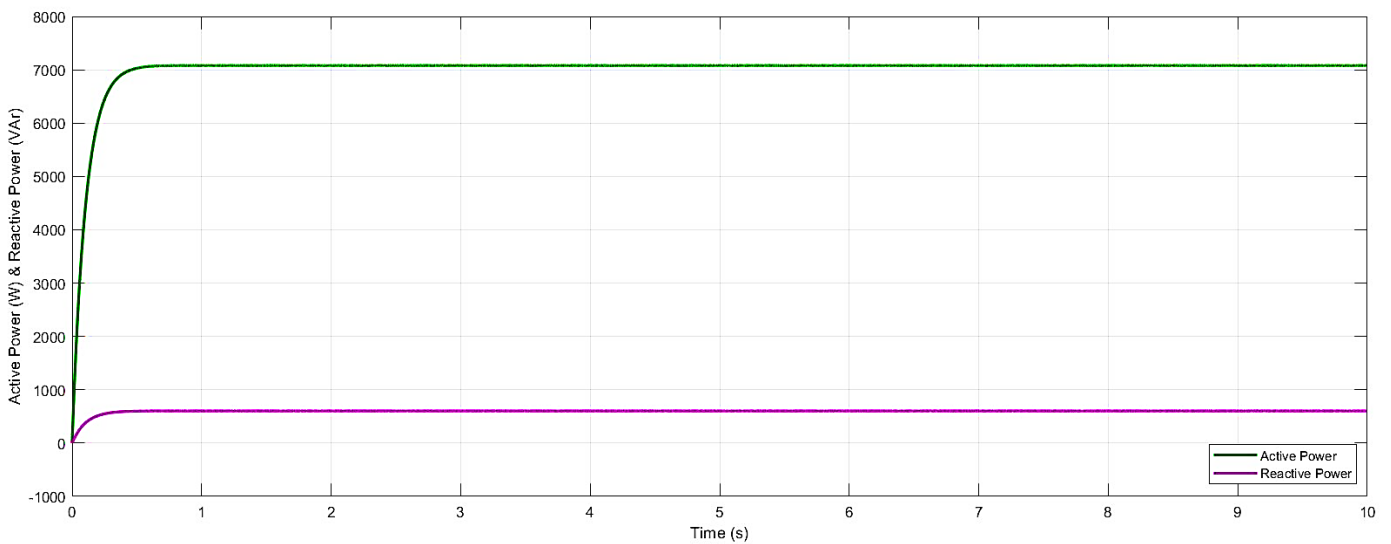


Fig. 17: Results of active and reactive power (Case Study 2)

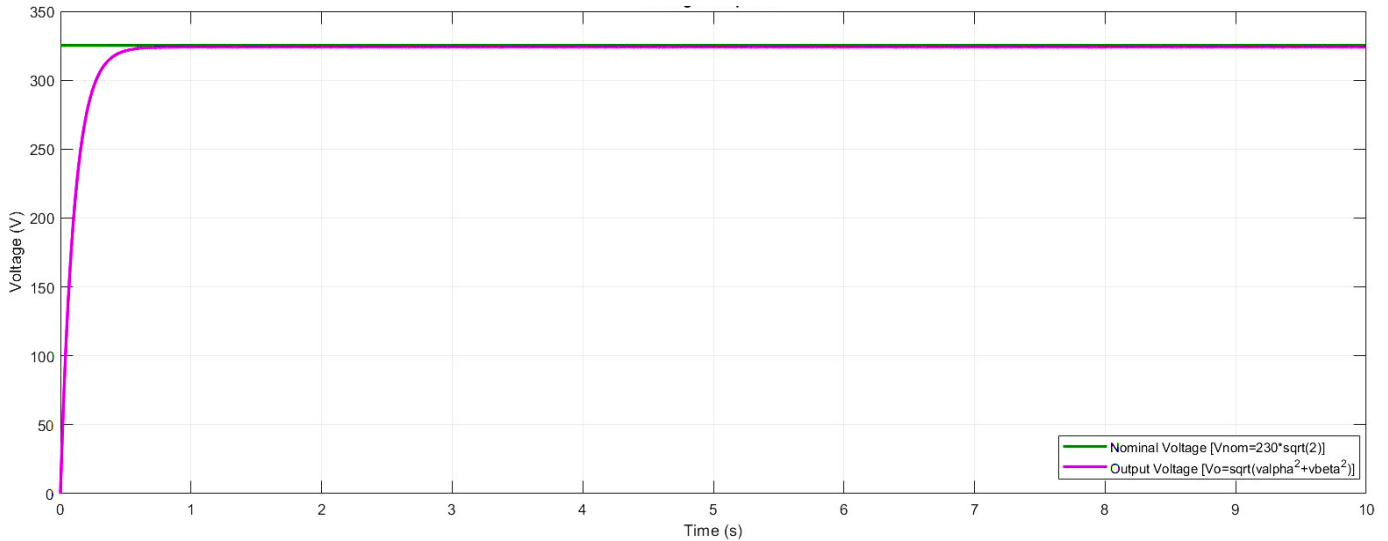


Fig. 18: Results of the nominal and output voltage (Case Study 2)

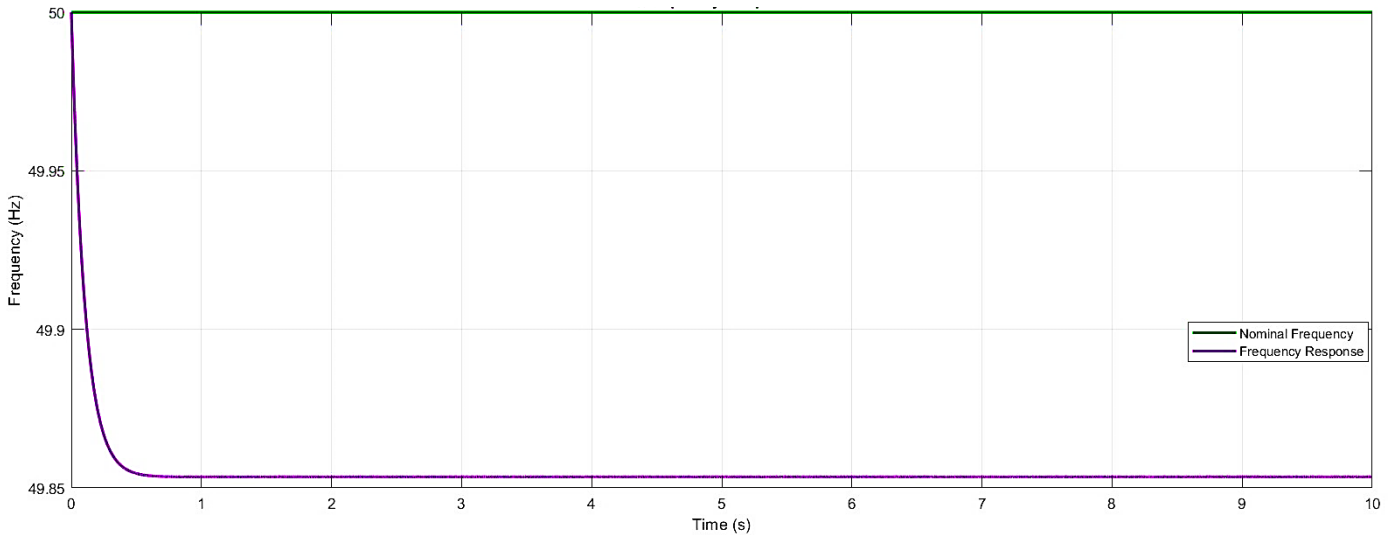


Fig. 19: Results of the output and nominal frequency (Case Study 2)

C- Third Case Study: The islanded (off-grid) mode microgrid composed by two renewable energy resources and two network converters and common home load (the primary control and the secondary control)

The third case study includes a multi renewable energy resource with maximum power point tracking control and one common load. In addition to the primary control that was applied in the second case study, the central secondary control is applied to restore the voltage and frequency deviations caused by the primary control. Table 5 shows the values of the second inverter. In addition to the control parameters applied in the previous case, Table 6 shows the parameters specified in the third case study. For the purpose of this case study, the designer model is similar to the second case study, including an additional wind turbine and converter, which will share the load with the former one after a specified period of time. Figure 20 shows a microgrid diagram of the third case study, which consisting of two

renewable energy resources and a common home (load). The inverters are arranged to connect to the microgrid progressively. Inverter 1 starts early, but inverter 2 starts after a certain time. The instant of time configured to trigger the second inverter. The second inverter is initially disabled and connected to the network after two seconds plus T_s , it connects to the grid maintaining this operation mode up to a time sufficient to demonstrate the steady-state response. Note that in this secondary control, inverter 1 is the central (master) control, and inverter 2 acts as a slave in this control method. The secondary control action is applied to reduce the voltage and frequency deviations. The PI compensator transfer functions performed in each loop to eliminate errors from comparison and standard voltage and frequency comparisons between the nominal and measured values of the voltage and frequency are described in Equation (35) and Equation (36).

$$PI_V(s) = \frac{K_{pv}s + K_{iv}}{s} \quad (35)$$

$$PI_f(s) = \frac{K_{pf}s + K_{if}}{s} \quad (36)$$

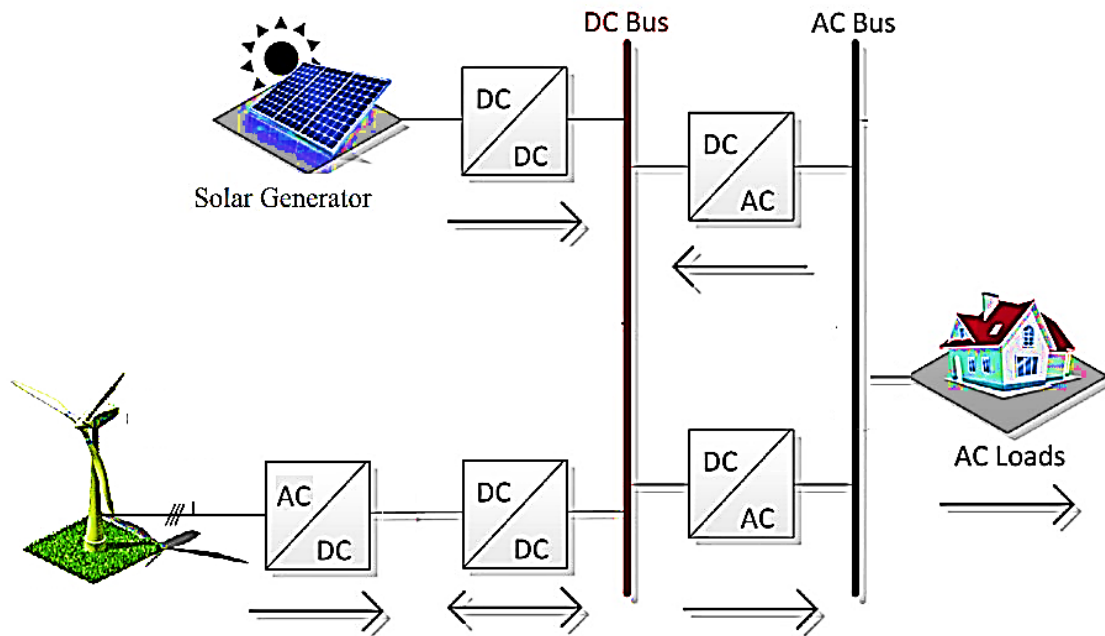


Fig. 20: The proposed system structure for the third case

TABLE 5
The Electrical Parameters of Microgrid in The Third Case Study

Parameter	Acronym	Value	Units
Output inductance	L_{o2}	6	m H
Output resistance	R_{o2}	0.6	Ω
LC filter capacitance	C_{f2}	12	F
LC filter damping resistor	R_{f2}	48	Ω
Line inductance	L_{L2}	1.2	m H
Line resistance	R_{L2}	78	m Ω

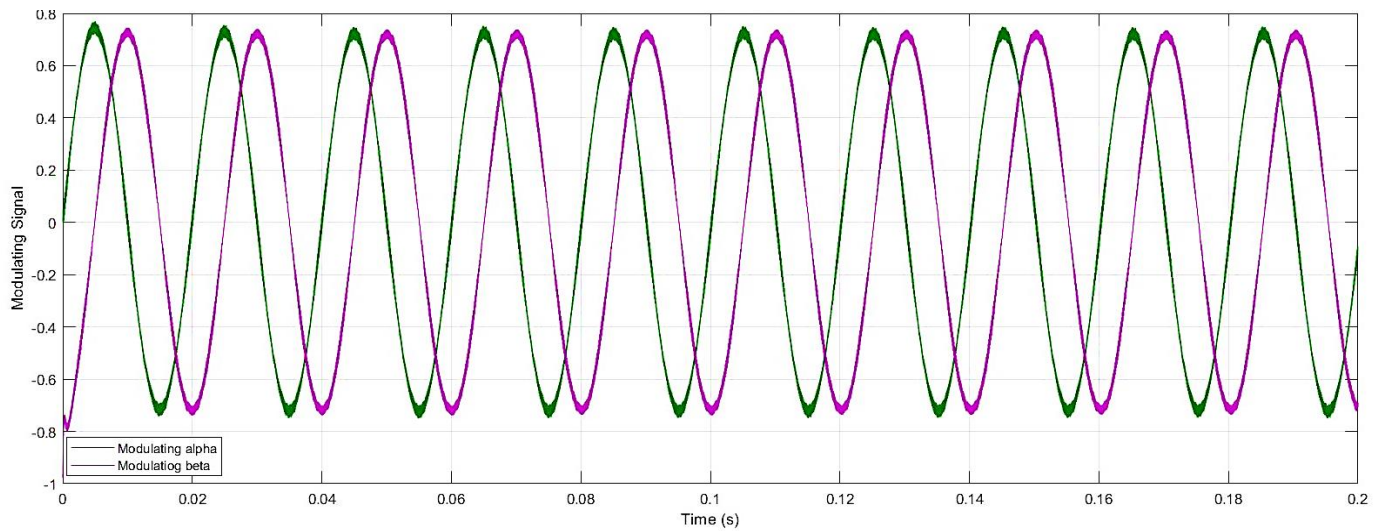
TABLE 6
The Control Parameters of The Microgrid in The Second Case Study

Parameter	Acronym	Value	Unit
Proportional gain PI voltage compensator	K_{pv}	0.1	A/V
Integral gain PI voltage compensator	K_{iv}	0.2	A^{-1}
Proportional gain PI frequency compensator	K_{pf}	0	A/V
Integral gain PI frequency compensator	K_{if}	10	A^{-1}

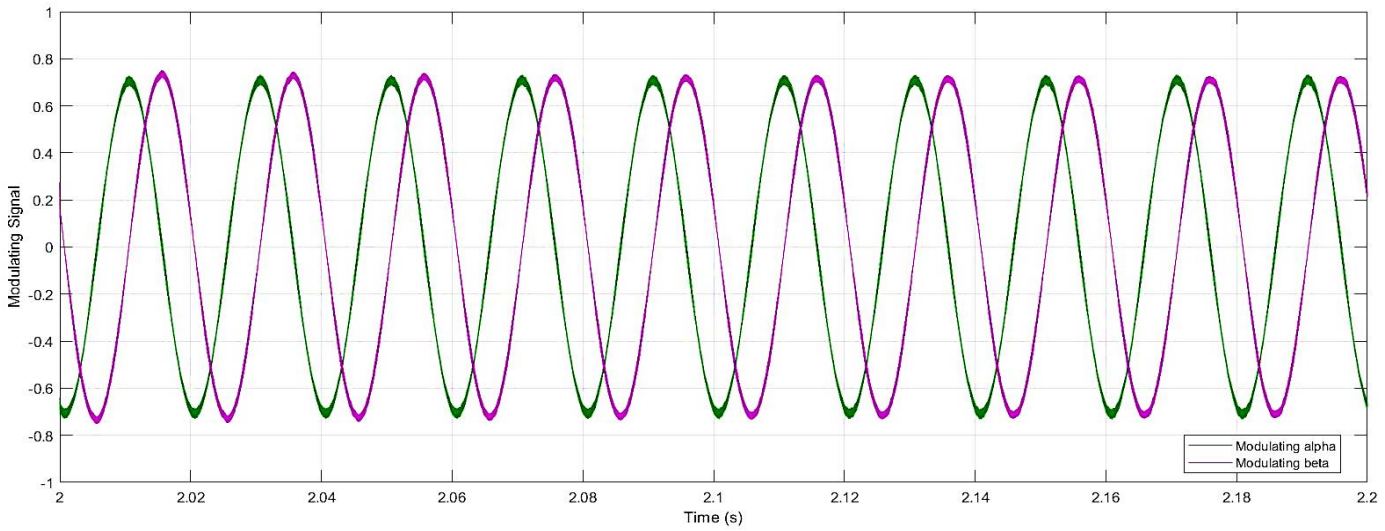
1. The Results of the Third Case

The results for the modulating, current and voltage tracking, reactive and active power, as well as the frequency and

voltage are demonstrated in Fig. 21, Fig. 22, Fig. 23, Fig. 24, Fig. 25, and Fig. 26.

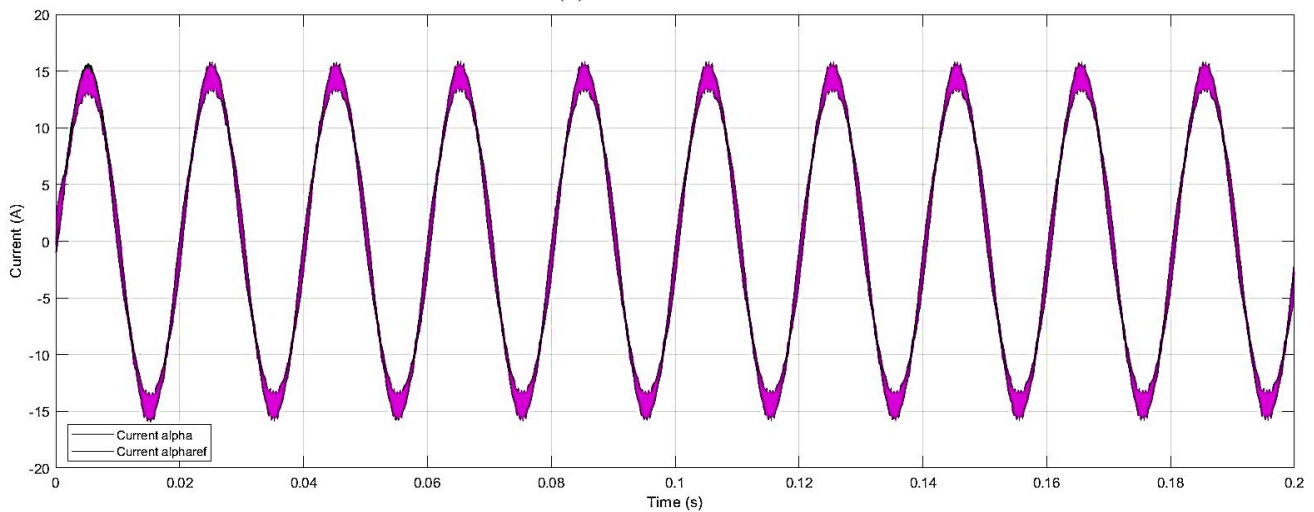


(a)



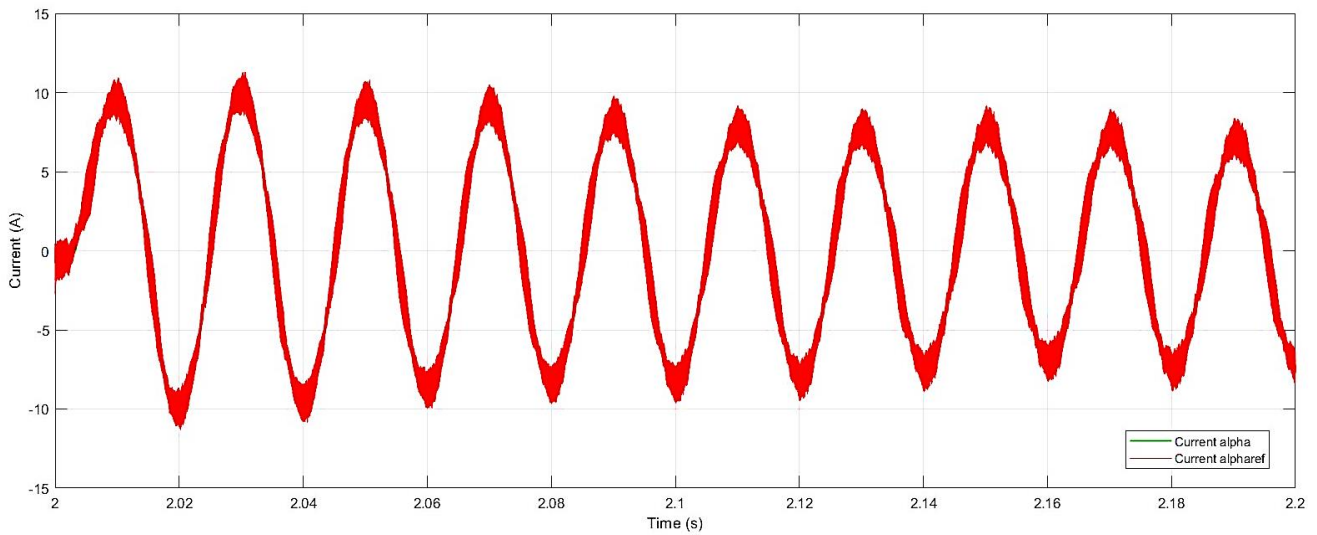
(b)

Fig. 21: The results of the modulating signals alpha and beta, (a) first inverter, (b) second inverter



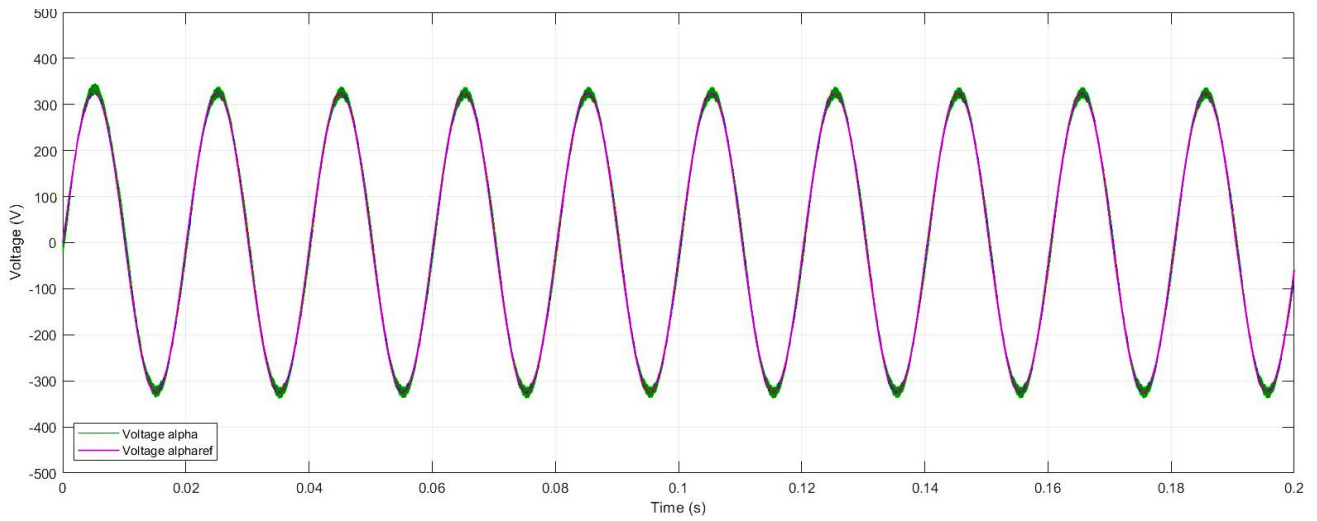
(a)

Fig. 22: The results of (a) Current tracking I-alpha and I-alpha ref for the first Inverter, (b) Current tracking I-alpha and I-alpha ref for the second Inverter

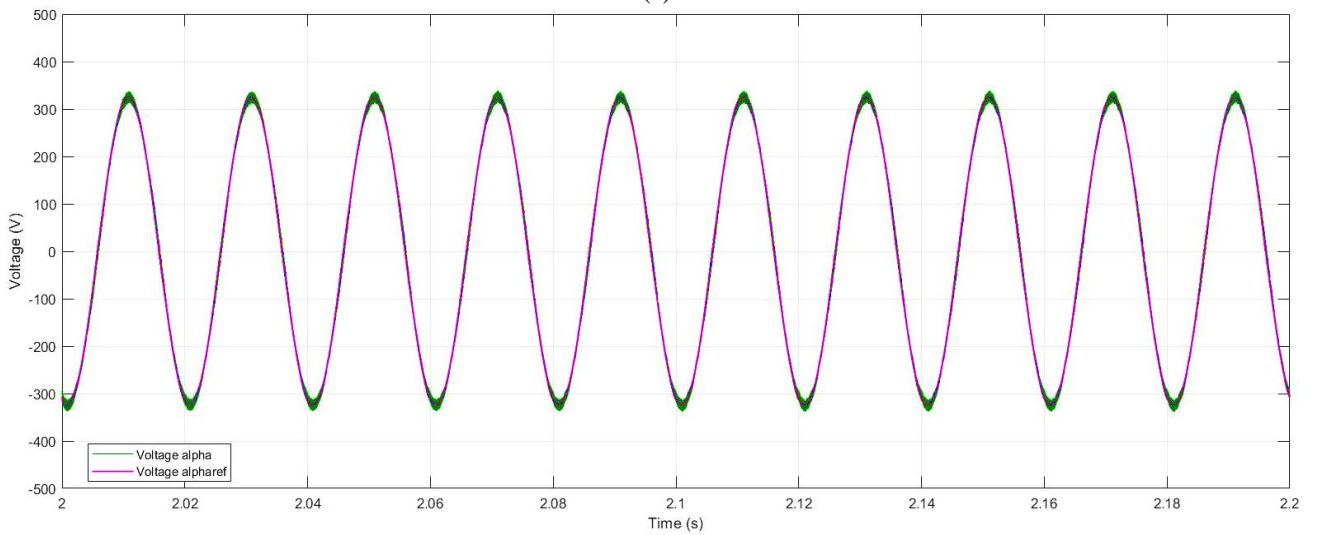


(b)

Fig. 22: Continued.



(a)



(b)

Fig. 23: The results, (a) Voltage tracking V-alpha and V-alpha_ref for first Inverter, (b) Voltage tracking V-alpha and V-alpha_ref for the second inverter.

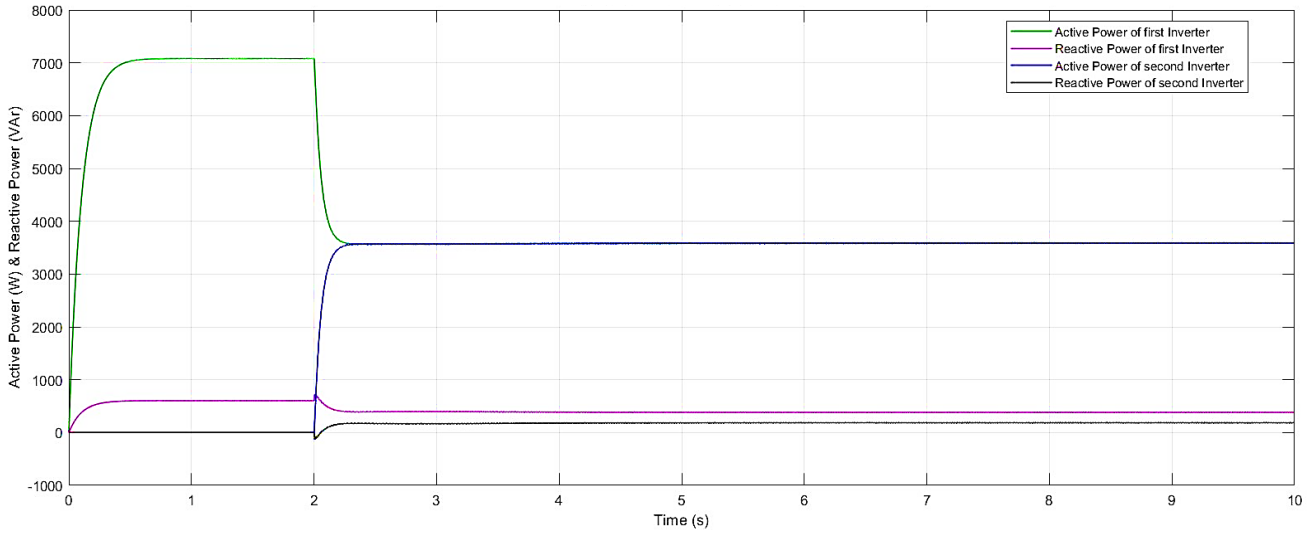


Fig. 24: The results of the reactive and active power

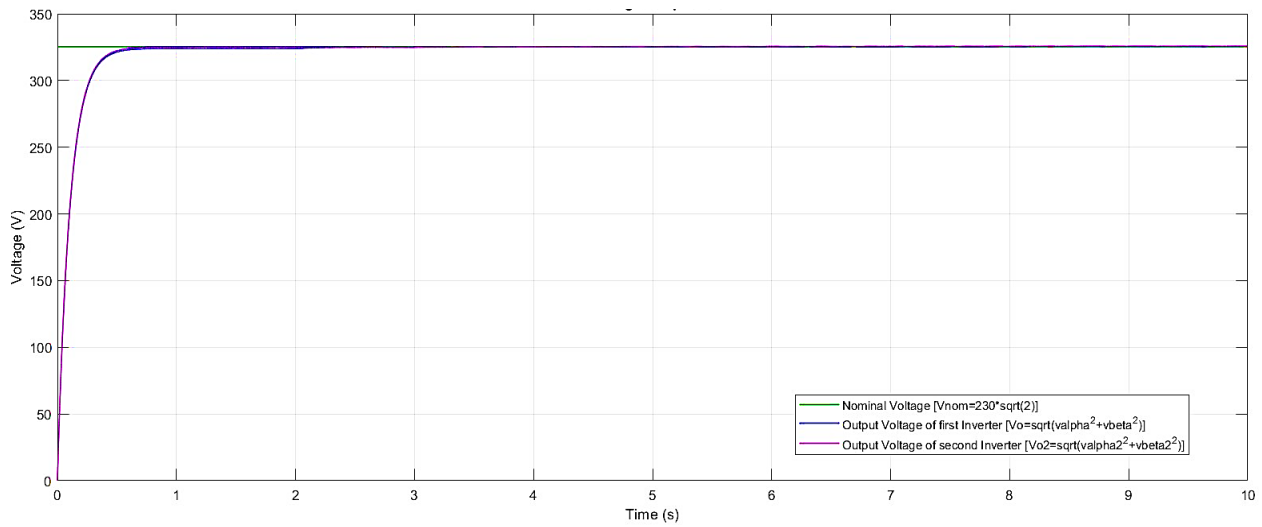


Fig. 25: The comparison between output and nominal voltage

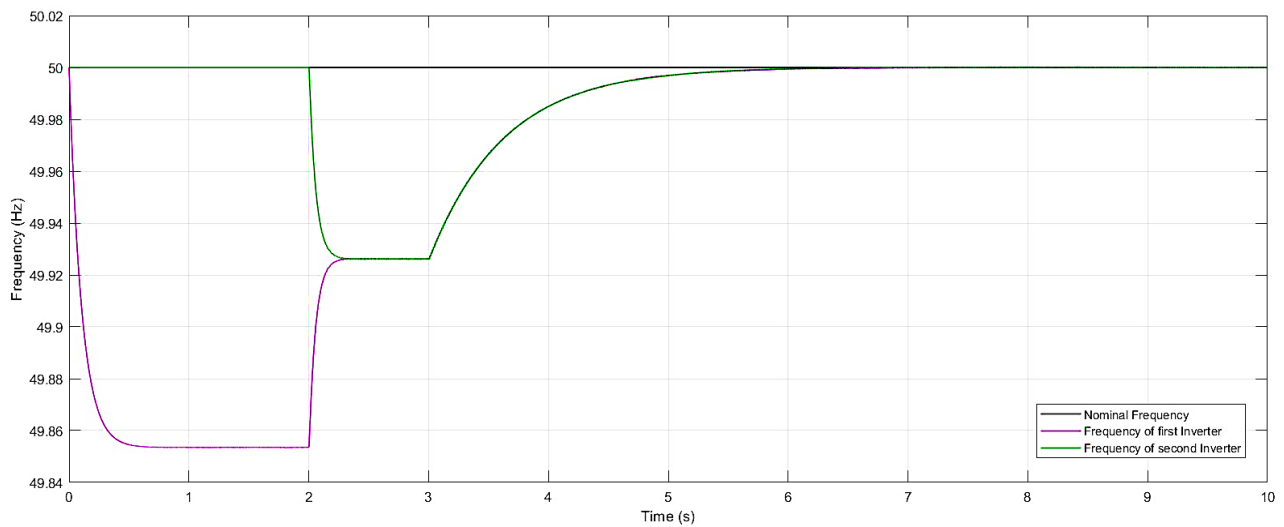


Fig. 26: The comparison between output and nominal frequency

Figure 24 illustrates the sharing of active and reactive energy between two reflectors on a microgrid network, obtained by the drooping control method. The first inverter starts automatically at $t = 0$ seconds and supplies all the required power. At $t = 2$ seconds, the second inverter starts sharing the power. As observed in the figure, the active power achieves ideal power-sharing because the frequency is a global variable, and all nodes in the microgrid show the same frequency. In contrast, the reactive power-sharing is not perfectly achieved because to the fact that the voltage amplitude is a local variable that presents different values at each node. Note that these power-sharing results were accomplished by considering perfect, lossless, and without any communication network constraints. The result obtained in Fig. 25 shows the stable operation of the proposed system, which reaches the nominal value of the voltage. Figure 26 validates the secondary control function of frequency restoration, providing an ideal transient response.

VII. CONCLUSIONS

In this paper, a new coordinated control strategy of hybrid AC/DC microgrid with photovoltaics and wind turbine sources is proposed. The main contribution of this work can be summarized as follows. At the local level, the interfaced power converters are controlled coordinately to control the output voltage and current. Specifically, a model predictive power and voltage control method is developed for the AC/DC interlinking converter to maintain stable AC/DC bus voltages and to facilitate the grid synchronization and connection. At the system level, energy management is developed to maintain the power balance under variable generation and consumption conditions. Also, in this work, coordinated control of hybrid microgrids with renewable energy resources shows the effectiveness of such a technique to deliver uninterrupted power to the consumer through various controller designs. In addition, in order to avoid the drawbacks of the conventional droop control, an improved droop control strategy based on integrator current-sharing is introduced. Also, the incremental conductance MPPT technique is applied for both photovoltaics stations and wind turbines to extract the maximum power from the hybrid power system. Various case studies under grid-connected, islanded and grid synchronization modes have validated the satisfactory performance of the microgrid architecture and the proposed control strategy.

CONFLICT OF INTEREST

The authors have no conflict of relevant interest to this article.

REFERENCES

- [1] X. Fang, M. Atyajayant, Y. Guoliang. "Smart Grid - The New and Improved Power Grid: a Survey". *Communications Surveys & Tutorials*, vol.4, pp. 103-110, 2012.
- [2] J. Gao, Y. Xiao, J. Liu, W. Liang, C. Chen, "A Survey of Communication/Networking in Smart Grids", *Future Generation Computer Systems*, vol.28, pp. 391-404, 2012.
- [3] I. Colak, E. Kabalci, G. Fulli, S. Lazarou, "A Survey On the Contributions of Power Electronics to Smart Grid Systems", *Renewable and Sustainable Energy Reviews*, vol. 47 pp. 45-57, 2015.
- [4] C. Mavrok, D. Ampeliotis, K. Berberidis, "A Study Of The Communication Needs In Micro-Grid Systems", *IEEE General Assembly and Scientific Symposium of the International Conference Union of Radio Science (URSI GASS)*, Canada, pp.19–26 Aug, 2017.
- [5] T. Ustun, C. Ozansoy, A. Zayegh, "Recent Developments in Microgrids and Example Cases Around the World—A Review", *Renewable and Sustainable Energy Reviews*, vol. 12, pp. 15-25, 2013.
- [6] T. Zhou, B. Francois, "Energy Management and Power Control Of A Hybrid Active Wind Generator For Distributed Power Generation And Grid Integration". *IEEE Transactions on Industrial Informatics*, Vol.58, pp.95–104, 2016.
- [7] L. Khanh, J. Seo, Y. Kim, D. Won, "Power-Management Strategies For A Grid-Connected PV-FC Hybrid System", *IEEE Transactions on Power Delivery*, vol. 25, pp.1874–82, 2015.
- [8] L. Xu, D. Chen, "Control and Operation of a DC Microgrid with Variable Generation and Energy Storage", *IEEE Transactions on Power Delivery*, vol. 26, 2513–22, 2018.
- [9] N. Diaz, A. Luna, J. Vasquez, and J. Guerrero, "Centralized Control Architecture for Coordination of Distributed Renewable Generation and Energy Storage in Islanded AC Microgrids," *IEEE Transactions on Power Electronics*, vol. 32, pp. 5202–5213, 2017.
- [10] A. Mortezaei, M. Simoes, M. Savaghebi, J. Guerrero, and A. Al-Durra, "Cooperative Control of Multi-Master-Slave Islanded Microgrid with Power Quality Enhancement Based On Conservative Power Theory", *IEEE Transactions on Smart Grid*, vol.28, pp. 1234-1244, 2016.
- [11] Y. Karimi, H. Oraee, M. S. Golsorkhi, and J. M. Guerrero, "Decentralized Method for Load Sharing and Power Management in a PV/Battery Hybrid Source Islanded Microgrid," *IEEE Transactions on Power Electronics*, vol. 32, no. 5, pp. 3525–3535, 2017.
- [12] H. Mahmood, D. Michaelson, and J. Jiang, "Strategies for Independent Deployment and Autonomous Control of PV and Battery Units In Islanded Microgrids," *IEEE Journal of Emerging and Selected Topics in Power Electronics*, vol. 3, pp. 742–755, 2015.
- [13] S. Adhikari and F. Li, "Coordinated VF and PQ Control of Solar Photovoltaic Generators with MPPT and Battery Storage in Microgrids," *IEEE Transactions on Smart Grid*, vol. 5, pp. 1270–1281, 2016.
- [14] S. Jamalaldin, S. Hakim, and H. Razak, "Damage Identification Using Experimental Modal Analysis and

- Adaptive Neuro-Fuzzy Interface System (ANFIS)", Conference Proceedings of the Society for Experimental Mechanics Series 30, Vol.5, pp.399-405, 2012.
- [15] B. Tarek, D. Said, and M. Benbouzid, "Maximum Power Point Tracking Control for Photovoltaic System Using Adaptive Neuro-Fuzzy", IEEE, 2013, 8th International Conference and Exhibition on Ecological Vehicles and Renewable Energies (EVER), pp. 1-7, 2013.
- [16] M. Mahdavi, J. Zhu, and S. Mekhilef, "An Adaptive Neuro-Fuzzy Controller for Maximum Power Point Tracking of Photovoltaic Systems", IEEE TENCON 2015-2015 IEEE Region10 Conference, pp.1-6, 2015.
- [17] M. Villalva, J. Gazoli, E. Ruppert, "Modeling and Circuit-Based Simulation of Photovoltaic Arrays", Brazilian Journal of Power Electronics, Vol. 14, No. 1, pp. 35-45, 2009.
- [18] K. Nounou, "Design of GA Sugeno Fuzzy Controller for Maximum Power Point and Sun Tracking in Solar Array Systems", Master Thesis, The Islamic University, Gaza, 2013.
- [19] A. Oskouei, R. Banaei, and M. Sabahi, "Hybrid PV/Wind System with Quinary Asymmetric Inverter Without Increasing DC-Link Number," Ain Shams Engineering Journal, vol. 7, pp. 579-592, 2016.
- [20] C. Vasquez, J. Guerrero, J. Miret, M. Castilla, "Hierarchical control of intelligent microgrids". IEEE Industrial Electronics Magazine, vol.4, pp.23–29, 2011.
- [21] J. Guerrero, M. Chandorkar, T. Lee, "Advanced Control Architectures for Intelligent Microgrids—Part I: Decentralized and Hierarchical Control", IEEE Transaction on Industrial Electronics, vol.60, pp. 1254–1262, 2012.
- [22] J. Guerrero, J. Vasquez, J. Matas, D. Vicuna, M. Castilla, "Hierarchical Control of Droop-Controlled AC and DC Microgrids", IEEE Transaction on Industrial Electronics, vol.58, pp.158–172, 2017.
- [23] P. Marti, M. Velasco, E. Martín, M. Castilla, "Performance Evaluation of Secondary Control Policies with Respect to Digital Communications Properties In Inverter-Based Islanded Microgrids". IEEE Transaction on Smart Grid, vol. 9, pp. 2192–2202, 2018.
- [24] Z. Cheng, J. Duan, M. Chow, "A Comparison of Advanced Microgrid Management Systems", IEEE Industrial Electronics Magazine, vol.12, pp. 6–24, 2018.
- [25] J. Guerrero, P. Loh, T. Lee, "Advanced Control Architectures for Intelligent Microgrids — Part II: Power Quality, Energy Storage, And AC/DC Microgrids", IEEE Transaction on Industrial Electronics, vol. 60, pp. 1263–1270, 2013.
- [26] J. Miret, D. Garcia, J. Vicuna, R. Guzman, A. Camacho, "A Flexible Experimental Laboratory for Distributed Generation Networks Based On Power Inverters". Energies vol. 10, pp. 1580- 1589, 2017.
- [27] J. Rey, P. Marti, M. Velasco, J. Miret, "Secondary Switched Control with No Communications for Islanded Microgrids". IEEE Transaction on Industrial Electronics, vol. 64, pp.8534–8545, 2018.
- [28] W. Duesterhoeft, M. Schulz, E. Clarke, "Determination of Instantaneous Currents and Voltages By Means Of Alpha, Beta, And Zero Components". IEEE Industrial Electronics Magazine, vol.70, pp.1248–1255, 2005.



Bilal Naji Alhasnawi was born in Al Samawah, Iraq in 1993. he received the B.S. in Electrical engineering from the University of Kufa, in 2015. he received the M.S. degrees in Electrical engineering from the University of Basrah, in 2018. he is also working toward his Ph.D. degree within the Electrical Engineering Department, College of Engineering, University of Basrah, Basrah, Iraq. His research interests Smart Grid Engineering, Control Theory, Renewable Energy Technologies, Electrical Power Engineering, Power Systems Analysis, Power Electronics, Power Converters, Isolated Microgrids, Droop control, hierarchical control, Microgrids Optimization, Energy Management, Photovoltaics, Distributed Generation, Wireless Sensor Network, Information, and Communication Technology, and Computer Engineering. He is an Active Reviewer of the IEEE ACCESS.



Dr. Basil H. Jasim. received the B.Sc and M.Sc degrees in Electrical Engineering and Control & Computers Engineering from the University of Basrah, Basrah, Iraq in 1995 and 1999 respectively. He also received his Ph.D. degree in the field of Control and Systems from the Basrah University, Iraq in 2007. He is currently an Assistant Professor at the University of Basrah. His teaching interests covering wide areas of modules across the department of Electrical Engineering, University of Basrah, include Intelligent Control Systems, Robust Control Systems, Microprocessor & Microcontrollers, and Industrial Automation. He currently serves as a co-editor of the Basrah Journal for Engineering Sciences. His research interests include Intelligent Control of Robotics, Computational Intelligence, Chaos & Nonlinear dynamics, Renewable electrical energy systems, and PLC applications in industrial and engineering education. Dr. Basil is a Senior Member of the IEEE.